Contents lists available at ScienceDirect

Carbon

journal homepage: http://ees.elsevier.com

Origin of high photoluminescence yield and high SERS sensitivity of nitrogen-doped graphene quantum dots

Ruma Das [a], Sumaiya Parveen [a], Abhilasha Bora [a], P.K. Giri [a,b,*]

[a] Department of Physics, Indian Institute of Technology Guwahati, Guwahati, 781039, India
[b] Centre for Nanotechnology, Indian Institute of Technology Guwahati, Guwahati, 781039, India

ARTICLE INFO

Article history:
Received 18 November 2019
Received in revised form 3 January 2020
Accepted 9 January 2020
Available online xxx

ABSTRACT

Herein, we elucidate the origin of high photoluminescence quantum yield (PL QY) and high surface-enhanced Raman scattering (SERS) sensitivity of in-situ nitrogen-doped graphene quantum dots (N-GQDs). We show that the doping of heteroatoms in GQDs facilitates the excited-state charge transfer and improved recombination in N-GQDs yielding a PL QY of ~34%. Our study reveals that growth of GQDs in dimethyformamide solvent enables the reduction of the nonradiative sites in N-GQDs and the rearrangement of the charge distribution in the graphitic plane. Further, we demonstrate N-GQDs as an efficient SERS substrate with an enhancement factor of 3.2×10^3 with 10^{-4} M RhB target, which is ~7-fold higher than the previous reports. The comparative studies of the SERS for undoped and N- and S-doped GQDs allow us to assess the contribution of the Förster resonant energy transfer (FRET) and chemical enhancement (CM) factors. Further, by controlling the functional groups of N-GQDs with vacuum annealing, and with different laser excitations, we isolate the contributions of CM and FRET, for the first time. The optimized N-GQDs exhibits a SERS detection limit of 10^{-10} M for RhB. Finally, N-GQDs combined with RhB is utilized to demonstrate a white light emitter with a CIE coordinate (0.30, 0.34).

1. Introduction

Zero dimensional graphene quantum dots (GQDs), including doped GQDs, have recently been developed as fascinating fluorescent materials with distinct advantages in various fields, such as optical sensing, SERS detection, optoelectronic devices, photoscience, bio-imaging and bio-medical applications due to their extraordinary optical and electrical properties [1–12]. Considerable research efforts have been focused on the fabrication of GQDs by various methods, e.g., hydrothermal/solvothermal treatment, pyrolysis, microwave irradiation, laser ablation, electrochemical etching, and chemical ablation [1,4,5,13,14]. For example, Tang et al. reported the synthesis of glucose-derived water-soluble crystalline GQDs by microwave-assisted hydrothermal method [4]. Li et al. used an electrochemical approach to grow doped GQDs [5]. The pyrolysis process was reported by Hu et al. for the synthesis of the functionalized carbon QDs (CQDs) [15]. Among different processes, hydrothermal/solvothermal methods were reported widely for the synthesis of GQDs [1,14,16]. Das et al. reported the synthesis of undoped GQDs by hydrothermal processes [1]. In previous reports, nitrogen (N) doped GQDs (N-GQDs) was synthesized by both hydrothermal [16] and solvothermal [14] methods. Wang et al. recently reported the preparation of sulfur (S) doped GQDs (S-GQDs) by hydrothermal process [17]. Moreover, solvothermal process was previously implemented for the synthesis of S, N co-doped GQDs [18]. With hydrothermal method, the doping of other elements, such as, selenium [19], boron [20] in GQDs was also reported. Recently, the study of the solvent effects on GQDs has attracted much attention [21,22]. Cushing et al. showed the change of the photoluminescence (PL) of graphene oxide (GO) in a polar and non-polar solvent [23]. Papaioannou's group reported excitation-dependent light emission for CQDs suspended in different solvents [24]. To clarify the effect of organic solvents on the functional groups of GQD, Sekiya et al. studied the optical properties of GQDs in thirteen different solvents [25]. It is notable that the effect of solvents was studied mostly on post-synthesized GQDs, which showed the variation in optical properties of GQDs mainly due to the screening effect, polarization effect of solvent as well as the modification of surface functional groups of GQDs [21,22,25,26].

* Corresponding author. Department of Physics, Indian Institute of Technology Guwahati, Guwahati, 781039, India.
E-mail address: giri@iitg.ac.in (P.K. Giri)

https://doi.org/10.1016/j.carbon.2020.01.030
0008-6223/

Gone et al. reported the formation of circular GQDs through the reduction of the epoxy group by quasi-ring formation [27]. Liu et al. described the formation of N-GQDs in dimethylformamide (DMF) medium by the nucleophilic reaction [21]. In the reported works, the reacting solvents were chosen mainly to serve the purpose of different types of doping or functionalization [1,14,21]. The synthesis of GQDs in dimethyl sulfoxide (DMSO) in ambient pressure leads to the edge functionalization of GQDs [26]. Though there have been several reports on the post-synthesis doping of graphene quantum dots (GQDs), there is a lack of understanding of the choice of solvent/doping for a specific application of GQDs. In this context, we present here a comparative study of GQDs synthesized in different solvents under identical conditions and the corresponding formation mechanism and a critical analysis of the origin of high photoluminescence quantum yield and its applications in surface-enhanced Raman spectroscopy (SERS) and light-emitting devices. SERS is a sophisticated optical technique involving spectral analysis and it enables label-free and ultra-sensitive detection of biological molecules and chemical species [3,28–30]. GQDs were recently reported as efficient SERS substrate for detecting target molecules due to their large specific surface areas and more accessible edges, which results in more effective adsorption of target molecules [3,31]. In the previous literature, the SERS enhancement on GQDs based substrates was reported as charge transfer or chemical interaction between target molecules and substrate [3,28,31]. However, there is no clarity on the individual contributions to SERS performance, as it is challenging to classify the type of interaction, charge transfer, and their individual contributions in the SERS enhancement. It is important to understand the contribution of each process to engineer the SERS performance of GQDs for ensuring applications.

In the present study, we synthesize GQDs in three different solvents: water, DMF and DMSO by the standard top-down method using GO as a precursor material. The control over functional groups and the dopants is achieved based on the synthesis medium, as the DMF results in nitrogen-doped GQDs (N-GQDs) and DMSO results in sulfur-doped GQDs (S-GQDs) and the associated change in functional groups. Based on the reaction medium, the formation mechanism of different types of GQDs is first clarified. We investigate the origin of high photoluminescence yield from N-GQDs using various spectroscopic tools. Next, the use of N-GQDs as an efficient surface-enhanced Raman scattering (SERS) substrate has been explored with target molecule rhodamine B (RhB) and we demonstrate a detection limit as low as 10^{-10} M RhB. Through careful control of functional groups using vacuum annealing, the individual contribution of functional groups and doping in the SERS enhancement through Förster resonance energy transfer (FRET) are discussed in detail. Additionally, with the help of different laser excitation, we estimate the individual contribution of the FRET and chemical enhancement in SERS effect with N-GQDs substrate. Finally, the highly fluorescent N-GQDs are used as an efficient light converter and implemented them for the fabrication of liquid phase white light-emitting diode (WLED) with the help of RhB molecules.

2. Materials and methods

2.1. Synthesis of undoped GQDs, N-GQDs, and S-GQDs

Undoped GQDs was prepared by the well-known hydrothermal route with the graphene oxide (GO) as a precursor material [1]. The synthesis of GO with a modified Hummers' method is discussed in section S1 (Supporting Information, SI†). In a typical synthesis process, 600 mg of GO powder was dispersed in 40 mL Milli-Q (MQ) water and sonicated for 30 min. Then, the GO solution was transferred into a Teflon lined autoclave (Berghof, BR-100) and heated at 220 °C for 12 h. After cooling down to room temperature, the solution was centrifuged at 10000 rpm and the transparent suspension was collected as GQDs.

On the other hand, N-GQDs and S-GQDs were synthesized by the solvothermal method. Typically, 600 mg of GO powder was dispersed in 40 mL of DMF (99%, Sigma-Aldrich) and DMSO (Sigma-Aldrich), respectively, and sonicated for 30 min for proper mixing. Then the respective solutions of GO were transferred into the Teflon lined autoclave and heated at 220 °C for 7 h. After cooling down at room temperature, the solutions were centrifuged at 10,000 rpm and the yellow suspension was collected as N-GQDs and S-GQDs. Afterward, the solution was evaporate d by heating at 90 °C and re-dispersed in MQ, following its preservation at 4 °C. The reaction scheme for the synthesis of various type of GQDs in different mediums summarized in Fig. 1. In the scheme, we have highlighted the typical groups that are later assigned to non-radiative and radiative recombination pathways in different types of GQDs. After the synthesis of GQDs, N-GQDs, and S-GQDs, the solution of each sample with a concentration of 0.2 mg/mL was prepared in MQ water for further characterizations.

2.2. SERS detection

For the use of undoped and doped GQDs as SERS substrates, 0.2 mg/mL GQDs solution for each sample was prepared in MQ water. The solutions of dye molecules, e.g. RhB and methyl blue (MB), were arranged with different concentrations in methanol. 10 μL of GQDs solution was first drop cast on cleaned Si (100) substrate at a constant temperature, 70 °C. After complete drying of the GQDs solution, 20 μL of dye solution was dropped on top of the GQD-coated Si substrate. For the detailed quantitative analysis and optimization, mainly 10^{-4} M concentration of dye solution was used.

2.3. Fabrication of liquid phase white light-emitting diode (WLED)

For the fabrication of liquid phase WLED, N-GQDs were used as light converting material. Commercially procured low-cost UV LED (396 nm) was put into a culture tube containing N-GQDs solution (0.4 mg/mL) and sealed with a glass slip to obtain a liquid phase LED. The same arrangement was implemented with the addition of 50 μM RhB solution in N-GQDs solution with volume ratio 1:5 for the purpose of improvement of the purity of white light.

2.4. Characterization techniques

Transmission electron microscopy (TEM) including high-resolution TEM imaging was carried out using a JEOL-JEM 2010 transmission electron microscope operated at 200 kV. High-angle annular dark-field (HAADF) images were obtained using a scanning transmission electron microscope (STEM) in aberration-correction mode (JEM 2100F, 200 kV) for high-resolution imaging of a few samples. The test samples were obtained by drop-casting the aqueous dispersion on a carbon-coated copper grid of 300 mesh (Pacific Grid, USA), followed by drying at 70 °C temperature. Atomic force microscopy (AFM) (Cypher, Oxford Instruments) image was acquired in a non-contact mode. X-ray diffraction (XRD) pattern was recorded with Rigaku RINT 2500 TTRAX-III using Cu K_α radiation with a scanning speed of 3°/min. X-ray photoelectron spectroscopy (XPS) measurement was carried out using a PHI X-tool automated photoelectron spectrometer (ULVAC-PHI, Japan) with an Al Kα X-ray beam (1486.6 eV) at a beam current of 20 mA for the analysis of the chemical compositions and chemical environment.

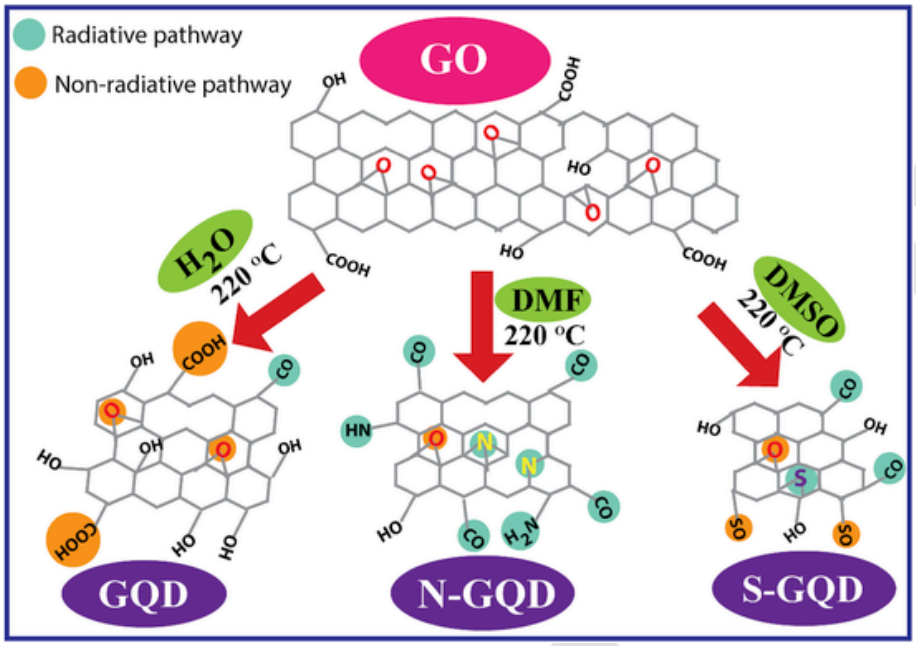

Fig. 1. Reaction scheme for the synthesis of different types of GQDs with different solvents. (A colour version of this figure can be viewed online.)

Raman scattering measurements were performed in a high-resolution Raman spectrometer (LabRam HR800, Jobin Yvon) with different laser excitations: 488, 514 and 633 nm. A 100X objective lens focused the laser beam with a spot size of ~1 μm in diameter. The acquisition time was 20 s for collecting the SERS spectrum. Fourier transform infrared (FTIR) spectroscopy measurements were executed in PerkinElmer, Spectrum BX spectrophotometer in the reflectance mode. For XRD, FTIR and Raman measurements, samples were dropped cast on Si(100) wafer, followed by drying at 70 °C. UV–Vis absorption spectra of the samples were recorded using the PerkinElmer spectrophotometer, Lamda 950. The steady-state photoluminescence (PL) measurements were carried out in a commercial spectrofluorometer (Horiba Jobin Yvon, Fluoromax-4) equipped with a Xe lamp source. Low temperature (80–300 K) PL measurements were carried out using a 405 nm laser excitation and a liquid nitrogen-cooled optical cryostat (Optistat DNV, Oxford Instruments) with the sample in a vacuum. Electroluminescence (EL) signal was acquired with the same spectrofluorometer using an external power supply. Time-resolved PL (TRPL) measurements were carried out with the excitation of a 405 nm laser source by a picosecond time-resolved luminescence spectrometer (FSP920, Edinburg Instruments) with an instrument response time of ~50 ps. The vacuum annealing was carried out in a quartz chamber for 2 h at different temperatures (200, 400 and 600 °C) under 2.5 × 10^{-2} mbar base pressure.

3. Results and discussions

3.1. Morphology and structural analysis

3.1.1. TEM and AFM analysis

The morphology of the as-synthesized GQDs was studied by TEM and AFM analyses. Fig. 2 shows typical plan-view TEM images and the size distributions of as-prepared GQDs, N-GQDs, and S-GQDs with the histogram in the respective insets. In the case of undoped GQDs, the average size of the GQDs is 4.0 nm, as shown by lognormal fitting in the inset of Fig. 2(a). Fig. 2(b) shows the HAADF TEM image of the N-GQDs and the upper inset shows the size distribution of N-GQDs with an average size of 3.0 nm. The lower inset of Fig. 2(b) shows the AFM image and the corresponding height profiles of the N-GQDs revealing its thickness as 0.6 nm corresponding to monolayer graphene oxide [32]. Fig. 2(c) shows the bright-field TEM image of S-GQDs with an average size of 2.2 nm, as shown in the corresponding inset. Thus, the average size of the GQDs gradually decreases with doping in the order of GQDs, N-GQDs, S-GQDs. Moreover, the histograms show that the size distribution follows a symmetric nature for undoped GQDs, while some asymmetry in the size distribution is observed for N-GQDs and S-GQDs. The HRTEM images of different GQDs in Fig. 2(d–f) exhibits the well-resolved lattice fringes confirming the crystalline nature. The 2D fast Fourier transform (FFT) pattern of the GQDs in the inset of Fig. 2(d) shows a standard six-fold symmetry of synthesized undoped GQDs. Further, the inverse fast Fourier transform (IFFT) of the HRTEM image of the selected area (yellow square) reveals the clear lattice fringes. The lattice spacing of 0.23 nm corresponding to (1120) hcp plane of GQDs [33] and 0.22 nm for (100) plane show the high crystalline nature of the as-grown GQDs [1]. The 2D FFT pattern of N-GQDs and S-GQDs in the inset of Fig. 2(e and f) show the gradual destruction of hexagonal structure with an approach towards amorphous nature after the doping of N or S atoms, consistent with the previous report [34]. The IFFT image of N-GQDs shows an interplanar spacing of 0.20 nm in (101) direction, while it is 0.19 nm in S-GQDs, which could be due to the compressive strain in S-GQDs.

3.1.2. XRD analysis

Fig. 3 shows the XRD pattern of undoped and doped GQDs. In each case, a strong diffraction peak corresponding to (002) graphitic plane appears together with few weak pea ks corresponding to (100), (101) and (004) planes, as indicated in Fig. 3. The (002) diffraction peak at 2θ ~26.0° is attributed to the presence of sp^2 hybridized carbon in the basal plane of GQDs [35]. Remarkably, the line width of the (002) peak of N-GQDs is lower than that of the other samples. This could be due to the reduced disorder/vacancy in the basal planes of N-GQDs, which will be confirmed later. Interestingly, the lowering of the 2θ values for the doped GQDs (N-GQDs and S-GQDs) indicates the expansion of interplanar spacing in the basal planes (see Fig. S1, SI†). The formation of GQDs in DMF and DMSO may dope N and S, respectively, in

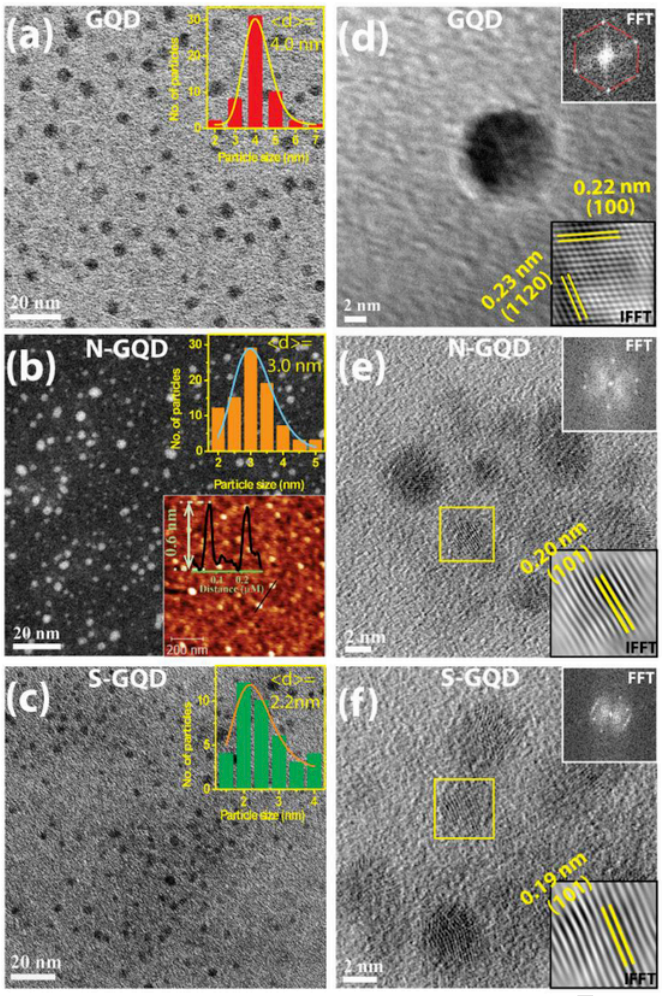

Fig. 2. TEM images of (a) GQDs, (b) N-GQDs and (c) S-GQDs, where, GQDs and S-GQDs are presented with bright-field images and N-GQDs with dark-field images. The upper insets show the particle size distribution of the respective samples. The lower inset in (b) shows the AFM image of N-GQDs with a height profile revealing the monolayer thickness of GQDs. (d) The HRTEM lattice image of a GQD; the upper inset shows the 2D FFT image of GQD with hexagonal lattice structure and the lower inset shows the IFFT image of the GQD. (e, f) HRTEM images of N-GQDs and S-GQDs, respectively; The upper inset in each case shows the 2D FFT image and the lower inset shows the IFFT image of selected GQD marked with yellow square. (A colour version of this figure can be viewed online.)

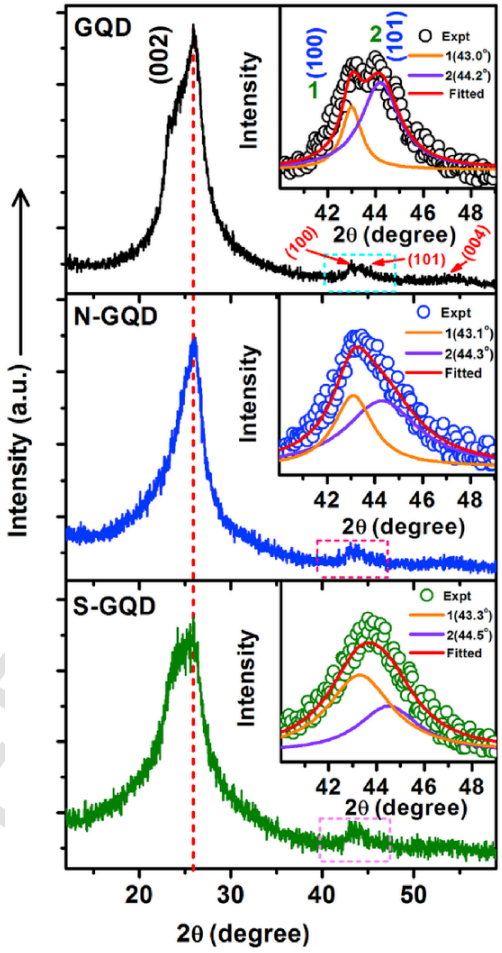

Fig. 3. Powder XRD pattern of undoped and doped GQDs. The inset in each case shows the deconvoluted peak in the range of 40–50°. The vertical line indicates the position of (002) peak in different samples. (A colour version of this figure can be viewed online.)

the sp^2 domains and thus carbon atoms could be replaced with N or S atoms, which could modify the interplanar spacing. In the case of S-GQDs, the replacement of the C atoms with bigger size S atoms may increase the d-spacing of graphitic planes. For a detailed analysis of the changes in the doping/defect induced planes in different GQDs, the XRD peak is deconvoluted with two Lorentz peaks in the range $2\theta = 40–50°$, as shown in the inset. The deconvoluted peaks 1 and 2 in each sample correspond to (100) and (101) planes [1,14,35]. The interplanar spacing of both (100) and (101) planes reduce after doping with N and S atoms. The increase in full-width half maxima (FWHM) of the deconvoluted peaks after doping (see Table S1, SI†) could be due to the attachment of excessive functional groups or creation of defects in graphitic structures, which may cause a compressive strain along the (100) and (101) planes of the doped GQDs, and this is consistent with the HRTEM analysis.

3.1.3. XPS analysis

An overview of the chemical composition of different samples is observed from the XP S survey scan shown in Fig. 4(a). Along with the presence of C 1s and O 1s peaks, the appearance of N 1s peak in N-GQDs and S 2p, S 2s peaks in S-GQDs confirm the doping of N and S atoms for the reaction in DMF and DMSO medium, respectively. The XPS analysis on N-GQDs and S-GQDs show the doping concentration of N and S as 7.9% and 16.9%, respectively, as presented in Table 1. The ratio of carbon to oxygen content (C/O) is 1.85, 3.60 and 1.69 for GQDs, N-GQDs, and S-GQDs, respectively, based on the XPS analysis, which reveals that O content is much less in N-GQDs as compared to the other samples. This is consistent with the report by León et al. for DMF treated GQDs [36]. Next, the high-resolution N 1s spectrum is deconvoluted to determine the different types of doped N, as shown in Fig. 4(b). The peak positions of deconvoluted curves of N 1s spectrum in N-GQDs (see Table S2, SI†) indicates the presence of pyridinic-N, pyrrolic-N and graphitic–N/N–H [16,18]. Note that the high percentage of pyrrolic-N in N-GQDs is due to the reaction tendency of DMF with the epoxy-functional groups of the GO to form tertiary N [18]. On the other hand, the S 2p XPS spectrum of S-GQDs shows two peaks located at 163.9 eV and 165.1 eV (see Fig. 4(c)), which are identified as $2p_{3/2}$ and $2p_{1/2}$ states of thiophene-S (-C-S-C-), due to spin-orbit coupling [35]. The peak located at 168.0 eV is due to

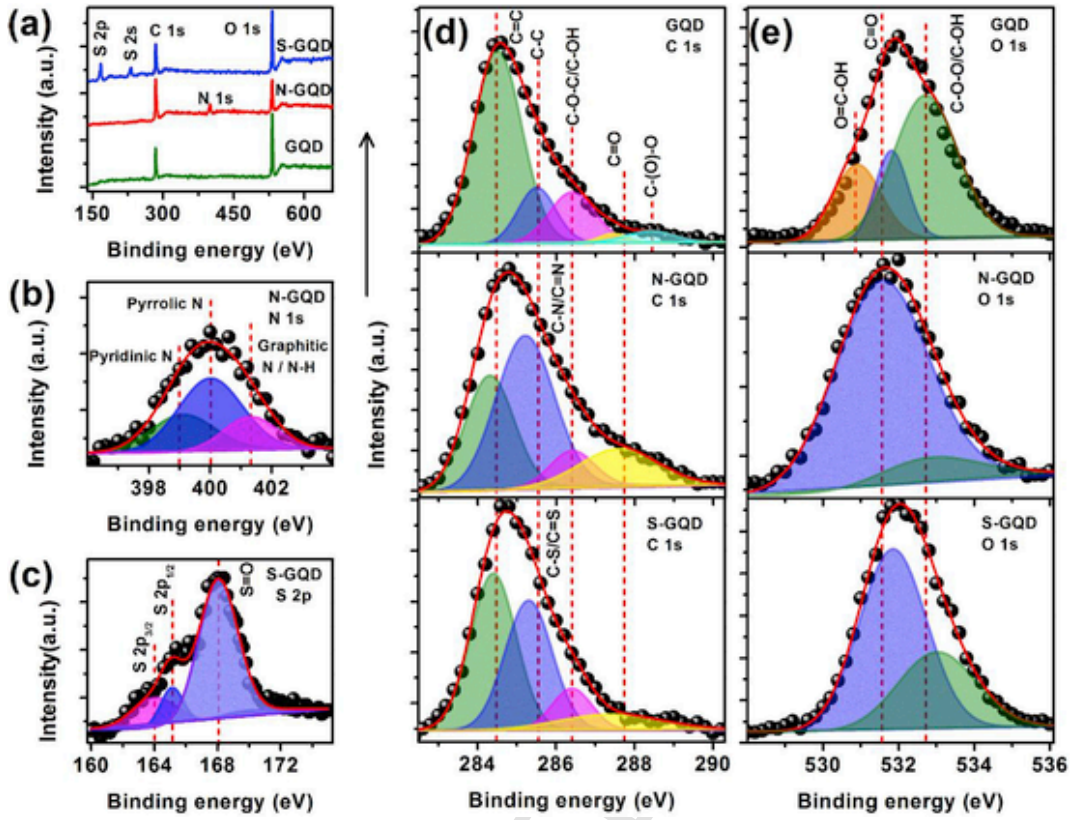

Fig. 4. (a) Survey scan XPS spectra for GQDs, N-GQDs, and S-GQDs. (b, c) High-resolution N 1s and S 2p XPS spectra of N-GQDs and S-GQDs, respectively. (d, e) Comparison of the C 1s and O 1s XPS spectra for undoped and doped GQDs. The symbols represent the experimental data and the solid lines indicate the fitted curves in each case. The vertical dashed lines indicate the respective peak positions in different samples. (A colour version of this figure can be viewed online.)

Table 1
Atomic concentration (%) of C, N, S, O in different types of GQDs, as revealed from the XPS analysis.

Sample	C (%)	O (%)	N (%)	S (%)
GQDs	64.9	35.1	–	–
N-GQDs	72.1	20	7.9	–
S-GQDs	52.3	30.9	–	16.9

the oxide S as the S═O group [18,35]. The oxide S in S-GQDs acquires 71% of the total sulfur content, indicating that most of S atoms exist as S═O functional group in S-GQDs. Thus, the doped sulfur in S-GQDs exists in two configurations: thiophene sulfur and oxide sulfur. Note that inside the autoclave, the DMF decomposes to electron-donating dimethylamine and carbon monoxide [37]. Dimethylamine, being a nucleophilic center, causes nucleophilic ring-opening reaction with the unstable epoxy groups of GO and extracts smaller sp^2 domains from the large GO sheets and simultaneously bonds with the aromatic ring to form N-GQDs [37]. Thus, the DMF can mainly introduce N content in N-GQDs as confirmed from the N 1s spectrum and it helps to reduce O content by cutting of GO sheets into smaller sp^2 domains. In contrast, in the case of DMSO, S and O can act as a nucleophile towards soft and hard electrophile, respectively. Thus, in the nucleophilic ring-opening reaction of GO, the epoxy group being a soft electrophile, is mainly affected by S center and thus S–O functional groups are directly attached at the edge sites, which enhances the O content in S-GQDs. Note that the water being a polar protic environment, it does not process any nucleophilic reaction. Gone et al. proposed the formation of GQDs by epoxy quasi-ring formation at high temperature and pressure reaction in water [27]. Mainly, the equilateral epoxy groups on the basal plane of GO create such a high strain that leads to the creation of fault lines and cracks in GO sheets [38]. Further, by the consecutive unzipping processes, circular-shaped GQDs are formed.

The deconvolution of C 1s spectra of different types of GQDs is presented in Fig. 4(d) and the summary of the changes with doping in different samples is presented in Table S2 (SI†). The presence of graphitic sp^2 hybridized carbon (C═C), sp^3 hybridized carbon (C–C) together with various oxygen functional groups (C–OH/C–O–C, C-(O)–O) are identified in GQDs [18,35]. Interestingly, for the case of N-GQDs and S-GQDs, the reduction of the binding energy of C═C is observed as a result of the doping in graphitic network with subsequent enhancement of the localization of electronic charge distribution in the sp^2 domains. Moreover, the deconvoluted peaks at 285.2 eV and 285.3 eV correspond to C–N/C═N and C–S/C═S bond in N-GQDs and S-GQDs, respectively [18], and that confirms the successful doping in respective samples. The maximum redshift of the binding energy of sp^3 carbon in N-GQDs endorses a higher electronic charge in C–N/C═N states. Note that the maximum contribution of C═C in GQDs (see Table S2, SI†) is attributed to the high crystallinity, while the dominating contribution of sp^3 carbon in N-GQDs and S-GQDs imply its disordered characteristics, which is consistent with HRTEM analysis. To be more precise about various oxygen functional groups of different samples, O 1s spectra are also deconvoluted, as presented in Fig. 4(e). Due to O═C–OH group, a peak at 530.9 eV is observed in GQDs [39], while there is no such peak in doped GQDs, which is consistent with the C 1s spectra. Qu et al. reported that the car-

boxylate groups could not be stable in the polar aprotic solution, while this group is stable in the polar protic environment, which is consistent with our results [40]. DMSO works as a mild oxidant and thus in the DMSO medium, the oxidation of hydroxyl groups to carbonyl can take place at high pressure and temperature reaction. In comparison to GQDs, the reduction of C–OH/C–O–C functional groups and the enhancement of the C═O groups for both N-GQDs and S-GQDs may be due to conversion of hydroxyl to carbonyl groups or higher number of ring-opening reaction with epoxy groups, as observed from C 1s and O 1s spectra in Fig. 4(d and e). Thus, the high content of C═O in N-GQDs is confirmed from both C 1s and O 1s spectra. Jin et al. reported that during the cutting of the GO sheet, epoxy chains on GO plane transform into carbonyl groups by oxidation [41], which is supporting our results. The change in the dopant and functional groups in N-GQDs and S-GQDs as compared to the undoped GQDs strongly influence the optical properties.

3.1.4. Raman spectral analysis

The extent of the disorder, the degree of crystallinity and doping induced changes in GQDs are investigated by Raman spectroscopy. The comparative Raman spectra of different types of GQDs are presented in Fig. 5(a) and the characteristics D, G, and 2D band positions are indicated by the vertical dashed lines. Fig. 5(b) shows the deconvolution of the Raman spectra in the region 1060 - 1650 cm^{-1} with Gaussian peaks and one Breit–Wigner–Fano (BWF) peak. The details of the peak parameters are presented in Table S3 (SI†). The characteristic G band at 1604 cm^{-1} in GQDs arises from the in-plane phonon vibration of sp^2 carbon [1,14]. With the introduction of doped atoms in the graphitic system, a significant redshift of the G band position is observed, as indicated in Fig. 5(b). Note that the redshifts of the G band are 11 cm^{-1} and 18 cm^{-1} for N-GQDs and S-GQDs, respectively, with respect to undoped GQDs. The redshift indicates a tensile strain in the lattice, which can be caused by the doped atoms, and this is consistent with the XRD analysis. In addition, the doping of electron-rich N or S atoms increases the electronic charge in N-GQDs and S-GQDs, as confirmed from C 1s XPS spectrum, may result in the redshift of G band. Moreover, from Fig. 5(a), the reduction of the intensity ratio of the 2D band to G band (I_{2D}/I_G) in doped GQDs is attributed to the enhancement of the electron concentration by N or S doping [42]. In the deconvoluted spectrum of GQDs, the D band appears at 1363 cm^{-1} due to the presence of defective sites. It has been reported that the D band in GQDs arises primarily due to the armchair edge sites [27]. In the present case, the values of I_D/I_G are 1.16, 1.40 and 1.19 for GQDs, N-GQDs, and S-GQDs, respectively. The higher I_D/I_G value in N-GQD reveals the higher density of Raman active edge sites and reduction in the crystallinity of the N-GQDs as compared to undoped GQDs. The higher density of edge sites N-GQDs is consistent with its smaller size than the undoped GQDs. Besides the characteristic G and D bands, the deconvolution of Raman spectra shows few additional Raman active bands corresponding to different functional groups named as D_1, D_2, and D_3, as listed in Table S3 (SI†). The D_2 band in GQDs represents the C–O vibration, whereas, D_1 and D_3 bands in doped GQDs correspond to the N or S doping as well as its attachment with various functional groups. The presence of the D_1 band in N-GQDs and S-GQDs is consistent with the higher contribution of sp^3 carbon in the C1s XPS spectrum. Interestingly, as compared to undoped GQDs, a gradual blue shift of the D bands is observed from N-GQDs to S-GQDs, caused by the compressive strain which is consistent with XRD analysis of (100) and (101) peaks. The presence of M peak with BWF line shape for each sample represents the metallic component of the GQDs [1]. The relative contribution of the M band in N-GQD (34%) is higher than that of S-GQD (30%). The higher intensity of the M band in N-GQDs indicates the presence of higher electronic charge in the graphitic network caused by N doping.

3.1.5. FTIR spectral analysis

The comparative FTIR spectra of undoped and doped GQDs are presented in Fig. 5(c). The absorption band at ~1650 cm^{-1}

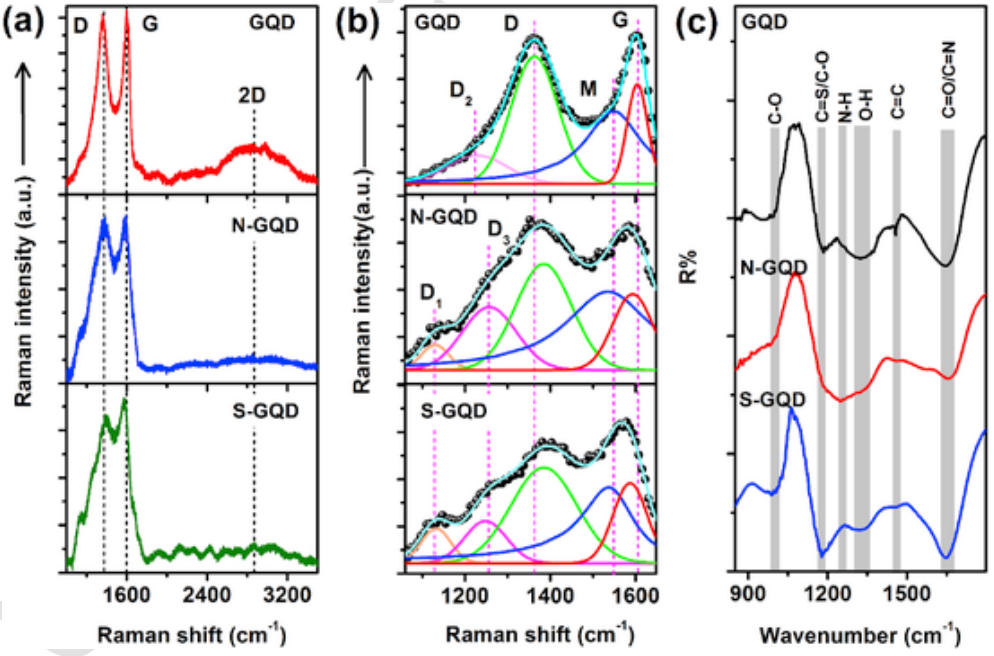

Fig. 5. (a) Comparative Raman spectra of GQDs, N-GQDs, and S-GQDs with 488 nm laser excitation. The vertical lines indicate the positions of D, G and 2D bands in GQDs. (b) Deconvolution of Raman spectrum of different samples with Gaussian peaks and a BWF peak (M) in the range 1060–1650 cm^{-1}. The symbol corresponds to the experimental data and the solid curves represent the fitted peaks in each case. The vertical lines indicate the shift of the peak positions in different samples. (c) Comparison of the FTIR spectra of GQDs, N-GQDs, and S-GQDs. (A colour version of this figure can be viewed online.)

and ~1240 cm^{-1} correspond to C═N and N–H vibrations, confirming the N doping and functional groups in N-GQDs [43,44]. The strong absorption band at ~1180 cm^{-1} is attributed to the stretching vibration of C═S indicating the successful doping of S atoms in the carbon network [18,35,45]. The strong absorption at ~1456 cm^{-1} in GQDs is characteristics of the stretching vibration of C═C in the aromatic skeleton [44], which is very week for S-GQDs and N-GQDs perhaps due to the doping effect. The absorption peaks at ~1000 cm^{-1} and ~1356 cm^{-1} in all samples are attributed to the stretching vibration of C–O and bending vibration of O–H due to the presence of oxygen functional groups [35,44].

3.2. Optical properties

The optical properties of GQDs are investigated with the help of UV–Vis absorption spectra, PL spectra at room temperature as well as low temperature (80 K) and time-resolved PL (TRPL) spectra.

3.2.1. UV–Vis absorption

Fig. 6(a) shows the comparative absorption spectra of GQDs, N-GQDs and S-GQDs. A deep UV absorption peak centered at ~265 nm in undoped GQDs is assigned to the characteristic π–π* transition within sp^2 hybridized carbon domains [1]. Note that the intensity of this peak is higher and the peak becomes broader in the doped samples. The higher intensity absorption implies the enhancement of the π–π* transitions in the core as a result of doping with electron-donating S and N atoms. Permatasari et al. reported that pyridinic-N of N-GQDs contribute a pair of electrons to sp^2 carbon (C) atoms [16] and Li et al. reported the donation of valence electrons of S atoms from their third shell to the graphitic domain [5]. These extra electrons probably cause higher absorption in the doped system. The absorption tail in the range 350–600 nm is assigned to the n–π* transition for the non-bonding electrons of O (C═O), N (C–N) and S (C–S) [14,18]. The Tauc plot in the inset of Fig. 6(a) shows that the indirect bandgap for N-GQD (2.08 eV) is much smaller than that of undoped GQDs (3.48). Jin et al. reported a reduction in the bandgap of N-GQDs with the increasing number of $–NH_2$ due to the donation of its lone pair electrons to the antibonding state in the benzene ring [41]. In the present case, the synthesis of N- GQDs in DMF solvent introduces electron-donating –NH groups in N-GQDs, which help to reduce their bandgap. For the case of S-GQDs, due to the presence of electron-withdrawing S═O functional groups, C–S/C═S are not able to enhance the electronic charge in sp^2 carbon efficiently. Thus, S-GQDs exhibit higher bandgap than that of N-GQDs.

3.2.2. PL excitation spectra

All the samples exhibit high PL emission with UV light excitations. The normalized PL excitation (PLE) spectra of all samples are presented in Fig. 6(b), which shows the position of the excitation maxima for different types of GQDs. Undoped GQDs and S-GQDs show the PLE peak at ~338 nm, while that of N-GQDs is at ~360 nm. A weak shoulder peak at ~272 nm in all samples is associated with the π–π* transition. Thus, the dominance of the 338/360 nm peak indicates a strong contribution of the functional groups/defects in the PL emission of all GQDs.

3.2.3. Room temperature PL study

Based on the PLE spectra, the PL spectra of undoped and doped GQDs are acquired and presented in Fig. 6(c). Note that the PL intensity of N-GQDs is much higher than that of undoped GQDs and S-GQDs. Hence the spectra are appropriately scaled to enable a better comparison. N-GQDs with an emission peak at 443 nm show

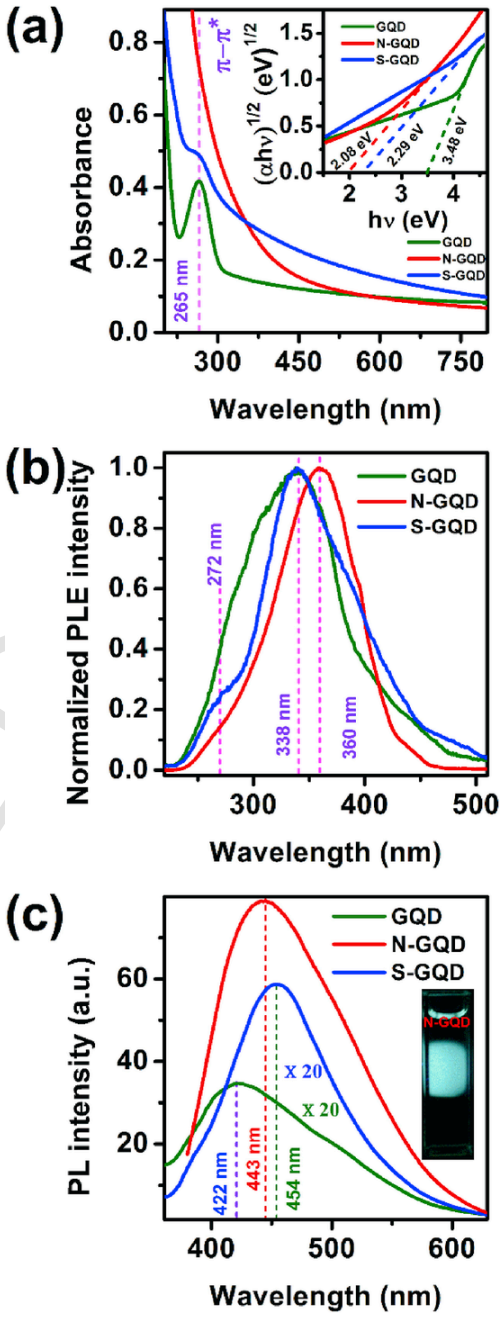

Fig. 6. (a) Comparative absorption spectra of GQDs, N-GQDs, and S-GQDs. The inset shows the Tauc plots with indirect bandgaps indicated in respective cases. (b) The normalized PLE spectra of undoped and N and S doped GQDs for emission at 422 nm, 443 nm, and 453 nm, respectively. (c) Comparative PL spectra of undoped and doped GQDs with the excitations at respective PLE maxima. The spectra of GQDs and S-GQDs are scaled up by a factor 20 to enable better comparison. The inset shows the digital photograph of N-GQDs dispersion with 360 nm excitation. (A colour version of this figure can be viewed online.)

~25 times stronger PL intensity than that of S-GQDs and the S-GQDs exhibits ~2 times higher PL intensity (at ~454 nm) than that of GQDs. A digital photograph of the N-GQDs with the illumination of 360 nm light is presented in the inset of Fig. 6(c), which shows strong bluish-green emission. The quantum yield (φ) of N-GQDs is measured as 34% with 0.05 M Quinine sulfate as a reference fluorophore [1]. For undoped GQDs and S-GQDs, φ values are 2% and 1%, respectively. Despite the higher PL intensity,

lower quantum yield in S-GQDs with respect to GQDs may be due to the higher absorption in S-GQDs. For comparison, the PL quantum yields of different GQDs are measured in DMF, DMSO and ethanol, and the results are shown in Table S4 (SI†). All the samples show relatively low quantum yield in DMSO medium as compared to other mediums due to the influence of S═O functional groups. The large PL enhancement in N-GQDs is owing to the presence of electron-donating N atoms and radiative surface functional groups. Due to the doping effect, the PL peak position redshifts by 21 nm and 32 nm for N-GQDs and S-GQDs, respectively, as compared to undoped GQDs. Yang et al. reported that lower electronegativity of S (2.51) than C (2.58) helps to increase the electronic charge in S-GQDs [2]. Although N has higher electronegativity than C, the presence of –NH groups/graphitic-N and pyridinic-N can increase the electronic charge in N-GQDs resulting in the redshift of the PL spectra as compared to GQDs [46]. To investigate the origin of different PL spectra of different samples, the excitation wavelength-dependent PL spectra were also acquired for all samples, as presented in Fig. S2 (a-c) (SI†). With increasing excitation wavelengths, all types of GQDs show a systematic redshift of the emission maxima. The excitation wavelength-dependent PL peak shift is usually attributed to the presence of multimission centers, which is a common feature of fluorescent carbon materials [46]. For a detailed analysis of the origin of emissive states in different types of GQDs, normalized PL spectra at excitations 300 nm and 370 nm are deconvoluted with multiple Gaussian peaks, as shown in Fig. 7 (a, b). The details of the deconvoluted peaks are presented in Table S5 (SI†). For GQDs, the PL spectrum under the excitation of 300 nm shows a dominating contribution of zigzag edge states [27] at ~410 nm, whereas, for doped GQDs, a large contribution is observed from of the doping states at ~ 440 nm/450 nm. Zhang et al. reported an emission peak at ~430 nm in N, S doped GQDs caused by the inherent surface states of multiple N and S containing functional groups [47]. Zhu et al. reported the emission peak at ~436 nm for the contribution of graphitic-N [43]. Base on our XPS analysis, in the present case, the deconvoluted peaks at ~440 nm and ~450 nm are attributed to the electron-hole recombination at C–N/C═N and C–S/C═S states in N-GQDs and S-GQDs, respectively. Along with the zigzag edge states, the presence of COOH and C═O functional groups in GQDs show emission peak at ~480 nm and 530 nm, respectively [27,47]. As we have observed the absence of COOH groups in XPS analysis for doped GQDs, no PL emission related to COOH groups in N-GQDs and S-GQDs again confirms the above assignment of PL peak. With higher excitation wavelength (λ_{ex} = 370 nm), the deconvoluted peak corresponding to different emission states is almost unchanged (see Table S4, SI†) when compared with λ_{ex} = 300 nm. In the case of higher λ_{ex}, the contribution of zigzag edge states diminishes and the doping states/functional groups dominate, which results in the overall redshift of the PL peak. It was reported that the presence of epoxy and carboxylic functional groups in GQDs induce non-radiative recombination of localized electron-hole pairs [2,6]. Thus, the presence of C–O–C/COOH surface functional groups in GQDs might be the main reason for low-intensity PL of undoped GQDs. Qu et al. reported the transformation of non-radiative COOH groups to radiative C–N/C═N centers with the N doping [40]. So, the doping of N/S could decrease the non-radiative sites in doped GQDs. Along with the reduction in non-radiative sites, the solvothermal reaction helps in the formation of radiative carbonyl (C═O) groups in N-GQDs and S-GQDs, as revealed from the XPS analysis. The presence of C═O groups and the absence of COOH groups in N-GQDs results in the extensive radiative recombination and thus high PL yield. In the case of S-GQDs, the existence of S═O functional groups reduces the effective n–π* transition. For the optimization of the N-doping density and PL intensity in GQDs, samples with different concentration of precursor GO (5 mg/mL,

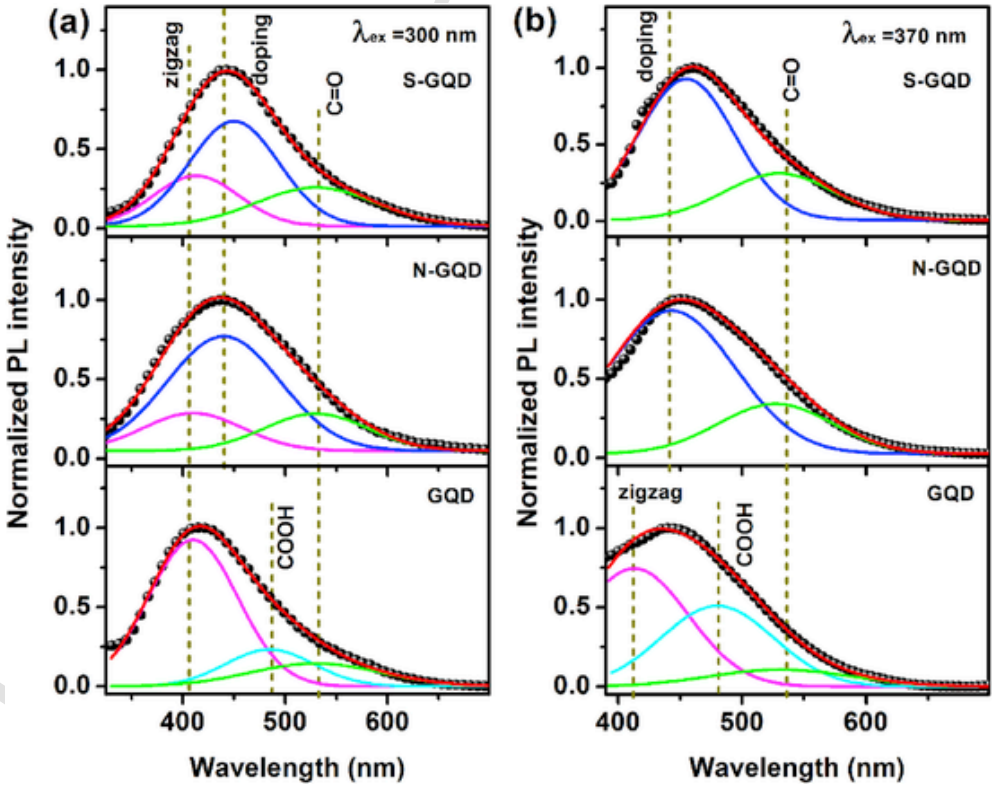

Fig. 7. Deconvolution of normalized PL spectra of GQDs, N-GQDs, and S-GQDs at the excitations 300 nm and 370 nm. The vertical lines indicate the peak positions. The symbols stand for the experimental data and the solid lines are for fitted curves. (A colour version of this figure can be viewed online.)

15 mg/mL and 20 mg/mL) was added with a fixed concentration of DMF, as shown in Fig. S3 (SI†). With a low concentration of GO, the PL intensity of N-GQDs is very low with the dominating contribution of oxygen-rich functional groups. At low GO concentration, the unreacted DMF could be attached to the surface of N-GQDs and increase the oxygen-related surface functional groups, which may reduce the electronic charge in the graphitic domains resulting in lower PL intensity. At a higher concentration of GO, the doping of N is not sufficient which again results in lower PL intensity (see Fig. S3, SI†)). Thus, the synthesis of N-GQDs with 15 mg/mL GO is optimized for efficient doping and strong PL emission.

3.2.4. Low-temperature PL study

To gain further insight into the emission mechanism, temperature-dependent PL spectra were acquired in the temperature range 80–300 K for different GQDs after drop-casting them on Si substrate. The temperature-dependent PL spectra of undoped and doped samples are shown in Fig. 8(a–c). As the temperature goes down from 300 K to 80 K, a monotonic increase in the PL intensity is observed in GQDs and N-GQDs indicating the positive thermal quenching (PTQ) phenomena [33]. At low temperatures, most of the carriers are frozen at the ground state and thus the photogenerated carriers recombine radiatively. With increasing temperature, the carriers acquire enough energy for escaping to higher energy levels and the possibility of the transition of these carriers in the non-radiative states increases, which results in PTQ. The changes of the integrated PL intensity with the inverse of temperature are shown in Fig. 8(d–f) for all samples. A quantitative analysis of the PQT is carried out with the well-known Arrhenius equation given by Refs. [48,49].

$$I(T) = \frac{I_0}{1 + Ae^{-\frac{E_a}{K_B T}}} \quad (1)$$

where I(T) and I_0 are integrated PL intensities at temperatures T K and 0 K, respectively. A is a constant, E_a is the activation energy for the non-radiative process, K_B is the Boltzmann's constant. To estimate E_a value for GQDs and N-GQDs, the experimental data are fitted with equation (1) in the higher temperature region (210–300 K), as shown at the corresponding inset of Fig. 8(d and e). The values of E_a are ~97 meV and ~171 meV for GQDs and N-GQDs, respectively. These results indicate that the required energy to activate the non-radiative channels in N-GQDs is very high as compared to GQDs, which suppresses the transition to non-radiative channels and most of the photogenerated carriers recombine through radiative channels with subsequent enhancement of the PL intensity in N-GQDs, consistent with the temperature-dependent intensity results. Due to the lower value of E_a, the transfer of photogenerated carriers to non-radiative states (defect, functional groups) is highly favorable in undoped GQDs. Dey et al. reported that at higher temperatures, a large number of excitons are relaxed through defect-related deep trap states, which act as non-ra-

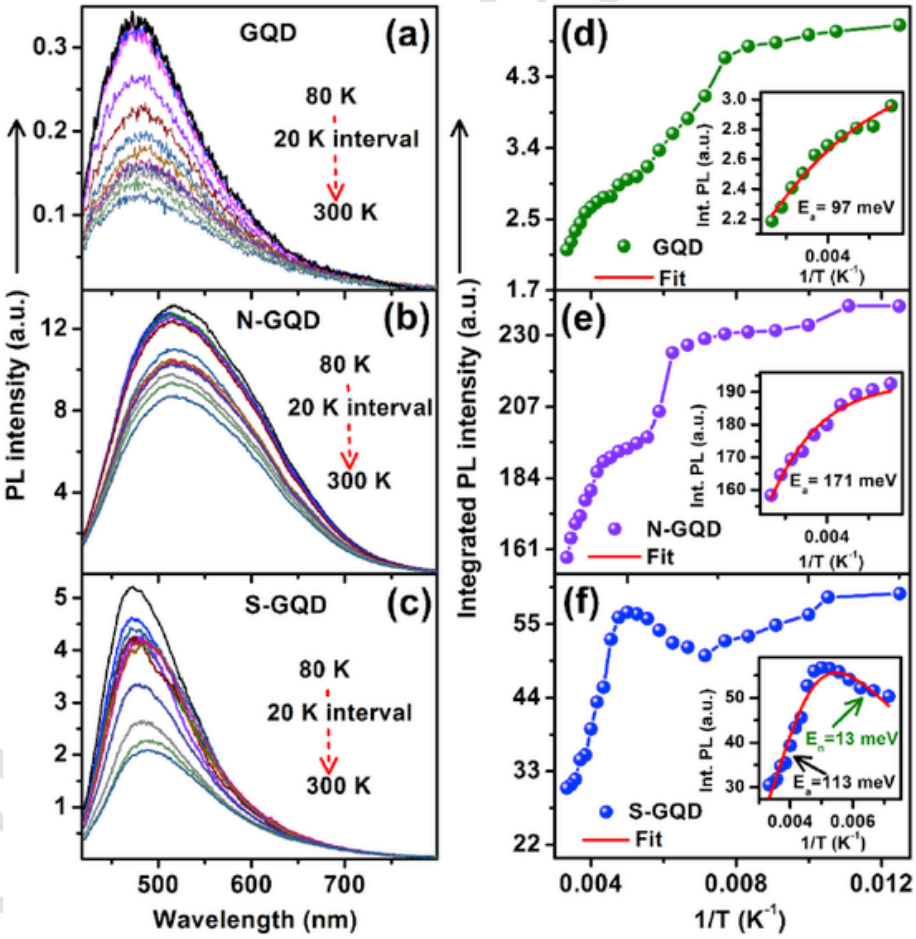

Fig. 8. Temperature-dependent PL spectra of (a) GQDs, (b) N-GQDs and (c) S-GQDs. (d–f) The corresponding variation of the integrated intensity of PL as a function of the inverse of temperature. The insets in (d) and (e) show the Arrhenius fitting in the higher temperature region (210–300 K for GQDs and N-GQDs. The inset in (e) shows modified Arrhenius fitting in the temperature range 140–300 K to show PTQ in cooperation with NTQ phenomenon. (A colour version of this figure can be viewed online.)

diative channels [33]. Noticeably, with the change of the temperature from 80 to 300 K, the reduction of PL intensities are 3.3 and 1.48 times for GQDs and N-GQDs, respectively. This result indicates that the high-intensity PL in N-GQDs is not only for the high activation energy but also for the presence of less number of non-radiative channels. Interestingly, for S-GQDs, PTQ behavior is observed in the range 80–130 K and 220–300 K. In the intermediate temperature range (140–210 K), the PL intensity of S-GQDs increases with increasing temperature, which is known as negative thermal quenching (NTQ). In the literature, NTQ was reported for GQDs [33] as well as N-GQDs [50] due to the thermal detrapping of localized exciton towards free exciton. To explain the PTQ in S-GQDs in cooperation with NTQ phenomena, the Arrhenius equation is modified as follows: [51]

$$I(T) = \frac{I_0}{1 + Ae^{-\frac{E_a}{K_B T}}} \times e^{-\frac{E_n}{K_B T}} \quad (2)$$

The additional term in equation (2) refers to the NTQ effect and E_n is the corresponding activation energy. The variation of integrated PL intensity with the inverse of T is fitted with a modified Arrhenius equation for S-GQDs in the region 140–300 K, as shown in the inset of Fig. 8(f) and the value of E_a and E_n are obtained as ~113 meV and ~13 meV, respectively. Santiago et al. observed NTQ phenomena in the case of N-GQDs and reported that at low temperature, charge carriers of the dopant induced states migrate to the nearby emitting states by overcoming intersystem barrier with energy 21 meV [50]. In the present case, for S-GQDs, the small activation energy (E_n = 13 meV) could be assigned as the intersystem barrier for S doped atoms. Dey et al. also reported that the relocation of charges from sp^2 to sp^3 sites of defective states is responsible for NTQ [33]. Note that in our case, GQDs and N-GQDs do not exhibit any NTQ behavior. Moreover, we have observed that in spite of the presence of electron-donating S atoms in S-GQDs, S-GQDs do not emit high-intensity PL as compared to N-GQDs. Thus, we conclude that the presence of high defect states (confirmed from XPS and Raman analysis) and dopant atoms create a high density of non-radiative sites that are mainly responsible for the low-intensity PL of S-GQDs at room temperature. Moreover, the low value of E_a in S-GQDs helps easy activation of the non-radiative process as compared to N-GQDs. In the comparison of GQDs and S-GQDs, the activation energy of S-GQDs may be due to the absence of COOH/OH functional groups, which are marked as non-radiative sites. For more detail insights, PL spectra at different temperatures are deconvoluted with two Gaussian peaks. The deconvoluted PL spectra of all samples at temperature 80 K and 300 K are presented in Figs. S4(a–c) (SI†). At higher temperature, a noticeable reduction of the intensity of peak 2 as compared to peak 1 in GQDs endorses that GQDs has a high density of non-radiative trapping states associated with surface functional groups among all other samples. It is interesting to note that two deconvoluted peaks exhibit a large redshift upon increasing temperature for GQDs and S-GQDs. For GQDs, Peak 1 and 2 show a redshift of 67 meV and 164 meV, respectively, while for S-GQDs, the corresponding shifts are 71 meV and 99 meV (see Figs. S5(a–c), SI†), revealing the exciton-phonon interaction [52]. During the nonradiative process, electronic energy is converted to the vibrational energy of the lattice, which causes the exciton-phonon coupling. The change in the line width (FWHM) of these two peaks with temperature is shown in Figs. S5(d–f) (SI†). The temperature-dependent variation of FWHM in GQDs and S-GQDs endorses the efficient energy transfer between core and surface state, while N-GQDs exhibits nearly temperature-independent behavior. Thus, the weak temperature effect in the PL spectra of N-GQDs confirms the dominating interaction mechanism as electron-electron interaction rather than electron-phonon coupling.

3.2.5. TRPL analysis

To investigate the recombination dynamics, TRPL spectra are recorded with 405 nm laser excitation. Each TRPL decay profile is fitted with a bi-exponential decay function given by: [1] $I(t) = \sum_{i=1}^{2} B_i e^{-\frac{t}{\tau_i}}$, where, I(t) is PL intensity at time t and B_i is the fractional intensity corresponding to decay time τ_i. Fig. S6 (SI†) shows the comparison of the TRPL spectra along with the fitted exponential for various samples. The details of the fitting parameters of the TRPL spectra are tabulated in Table S6 (SI†). The average lifetimes (τ_{avg}) for GQDs, N-GQDs, and S-GQDs are estimated to be 3.36 ns, 7.58 ns, and 4.53 ns, respectively. Two decay components in each sample corresponding to emission from two energy states, consistent with the steady-state PL analysis (see Fig. 7(b)). The fast decay component (τ_1) with lower amplitude (~25%) can be assigned to the functional groups and the slow component (τ_2) with higher amplitude (~75%) is attributed to doping induced states. Since the doping induced state contributes the maximum in N-GQDs, it shows the highest amplitude in the TRPL profile (see Table S6, SI†)

3.3. Application of N-GQDs as SERS substrates

Next, we analyze the performance of the undoped and doped GQDs as SERS substrates for the detection of the ultra-low concentration of RhB in nM level. The SERS effects on GQDs, N-GQDs, and S-GQDs substrates are first measured with 514 nm laser excitation in the presence of 10^{-4} M RhB, as shown in Fig. 9(a). Interestingly, a significant enhancement in Raman peaks of RhB at 1648 cm^{-1}, 1507 cm^{-1}, 1359 cm^{-1}, 1188 cm^{-1}, and 766 cm^{-1} are observed on N-GQDs substrate and a tiny signal appears at 1648 cm^{-1}, 1507 cm^{-1} with GQDs substrate, while S-GQDs do not show any measurable SERS signal. Huh et al. reported that ozone-induced oxidation in graphene improves the SERS signals [28], while Liu et al. recently proved that the oxygen-rich functional groups in GQDs diminish the SERS enhancement [3]. In the present study, we have observed the highest SERS signal with N-GQDs, which is probably facilitated by the reduction of non-radiative oxygen-containing functional groups in N-GQDs. Based on the high SERS signal, N-GQDs coated on Si substrate are optimized with different laser excitation wavelengths. Fig. 9(b) shows the Raman signal of RhB (10^{-4} M) at laser excitations 488, 514 and 633 nm, which clearly demonstrates the highest enhancement of the SERS signal with 488 nm laser excitation. With 488 nm excitation, different Raman modes of RhB (10^{-2} M) on Si substrate are shown in Fig. S7(a) (SI†). As a reference at 488 nm laser excitation, the enhancement factor (EF) for N-GQDs is calculated as 3.2×10^3 at 10^{-4} M concentration of RhB for 1648 cm^{-1} peak. The detail of the EF calculation is presented in section S2 (SI†). Recently, plasma-enhanced chemical vapor deposition (PECVD) grown GQDs exhibited an EF of 4.37×10^2 for 1648 cm^{-1} peak of R6G at 532 nm excitation [3]. Cheng et al. reported EF value of 6.9×10^1 for 1648 cm^{-1} R6G peak at 633 nm laser excitation [31]. Thus, the enhancement factor for our N-GQDs is the highest among the reported values without plasmonic components and it is about seven times higher than that of GQDs prepared by a sophisticated PECVD method. A comparison of SERS performance of different carbon-based non-plasmonic and plasmonic substrates with the present work is presented in Table S7 (SI†). Thus, the N-GQDs can indeed serve as a non-plasmonic robust SERS substrate with appropriate excitation energy.

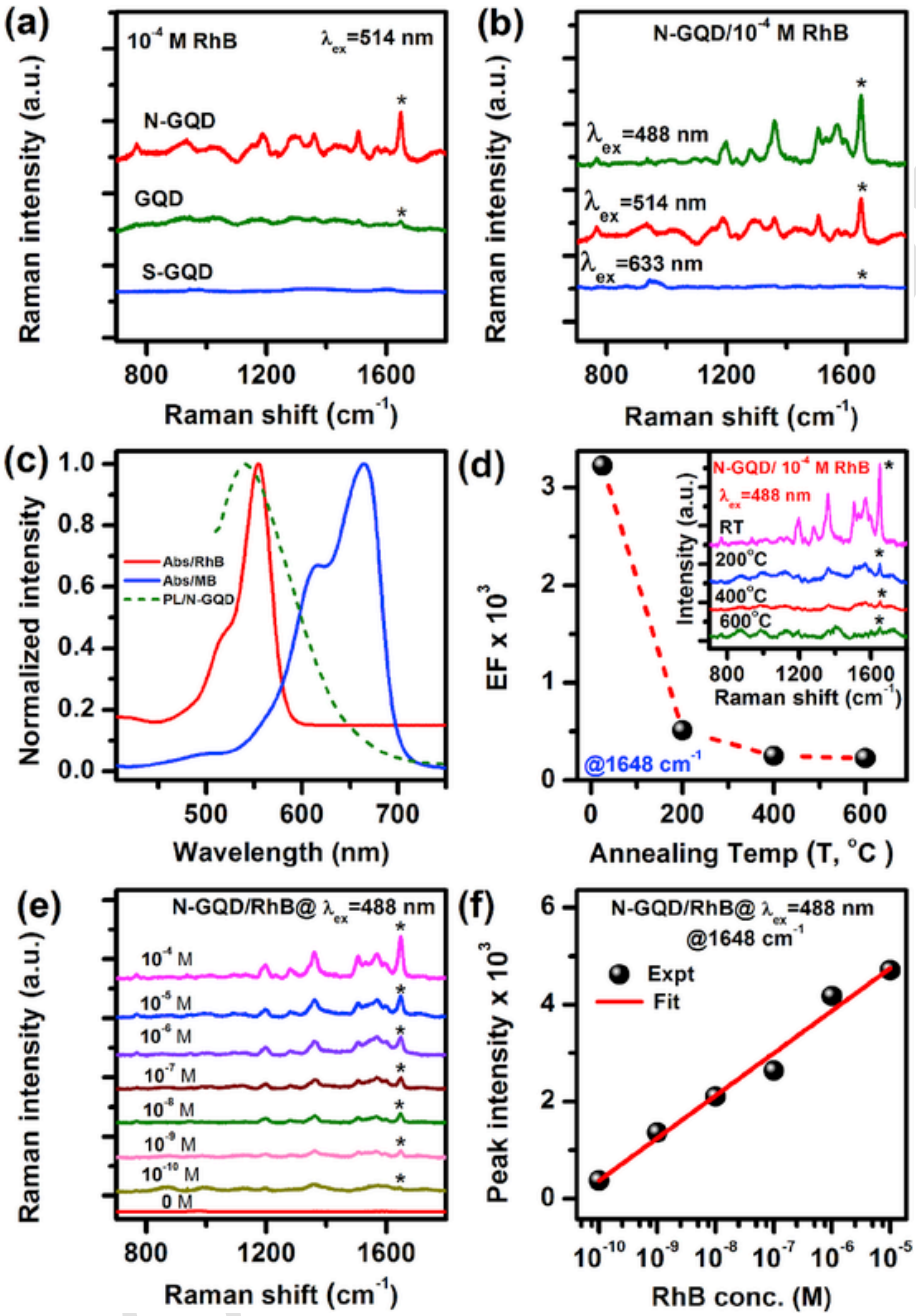

Fig. 9. (a) Raman spectra of RhB (10^{-4} M) using GQDs, N-GQDs, and S-GQDs as SERS substrates with laser excitation 514 nm. (b) SERS effect at different laser excitation wavelengths for 10^{-4} M RhB on N-GQDs substrate. (c) Normalized PL spectrum of N-GQDs (0.2 mg/mL) with excitation 488 nm and the absorption spectra of RhB and MB with concentration 10^{-5} M. The overlap of spectra indicates the possibility of FRET between N-GQDs and RhB. (d) The decay of the EF value at 1648 cm^{-1} of 10^{-4} M RhB on N-GQDs substrates prepared with different annealing temperatures and the corresponding Raman spectra are shown in the inset. (e) Concentration-dependent changes in the SERS signal intensity of RhB target on N-GQDs substrate. (f) The variation of Raman intensity of 1648 cm^{-1} peak with RhB concentration shows a linear variation in the range 10^{-10}-10^{-5} M '*' sign indicates the SERS enhanced peak of RhB at 1648 cm^{-1}. (A colour version of this figure can be viewed online.)

3.3.1. Mechanism of SERS enhancement

The SERS enhancement mechanisms are reported mainly to be contributed by the electromagnetic enhancement (EM) and chemical enhancement (CM) factors, where EM arises due to the localized electromagnetic field mainly in the presence of metallic components and CM involves the charge transfer phenomena [3,31]. Ling et al. reported that the π–π staking between the graphene and absorbed molecules could shorten the distance between the molecules and the substrate, which could facilitate an efficient charge transfer from substrate to target molecules [53]. For GQDs, larger surface areas with more accessible edges and dangling bonds can lead to more effective adsorption of target molecules. Liu et al. described the dangling bonds in GQDs as hot spots to adsorb or trap R6B molecules [3]. Nevertheless, the π–π staking is not the only factor that affects the SERS signal in graphitic materials. Ren et al. reported the SERS enhancement by electrostatic interaction of GO/Ag nanoparticle hybrids and folic acid [54]. In the present case, the possible reasons for the performance of N-GQDs as efficient SERS substrate are as follows. Among all syn-

thesized GQDs, the sp^2 domain in N-GQDs acquires higher electronic charge contents, which facilities maximum charge transfer to the target molecules by π–π interaction. Due to the high absorption of RhB, the strongest SERS signal was observed previously with 514 nm laser excitation [55]. In the present case, 488 nm laser excitation shows a higher efficiency than 514 nm for SERS enhancement. This is very likely to be related to Förster resonance energy transfer (FRET) from N-GQDs to RhB. Swathi et al. theoretically studied a fast resonance energy transfer process from dyes to graphene [56]. To clarify the contribution of the FRET process with RhB, the MB target (concentration 10^{-3} M) is also tested on the different types of GQDs for the SERS effect with 488 nm excitation, as shown in Fig. S7(b) (SI†). Although MB has an aromatic structure, a low EF value of SERS signal is observed with all kinds of the GQDs substrate, which reveals that the π–π interaction is not the only reason for SERS signal in N-GQDs. Interestingly, the PL emission peak of N-GQDs (at excitation 488 nm) coincides with the absorption peak of RhB, while the absorption peak of MB is far away, as shown in Fig. 9(c). Thus, due to overlap of the emission energy of donor (N-GQDs) with the absorption energy of acceptor molecule (RhB), and their close interaction, FRET is most likely to take place between N-GQDs and RhB. Thus, 488 nm excitation shows the highest EF in this donor-acceptor pair and the EF mechanism is essentially of chemical nature i.e., CM type. Note that among differently prepared N-GQDs substrates, N-GQDs prepared with 15 mg/mL GO concentration shows the maximum enhancement (see Fig. S7(c), SI†). Interestingly, the same sample shows the highest PL intensity as well. This reveals the excited-state charge/energy transfer from N-GQDs to target molecules (RhB) is primarily responsible for the SERS enhancement in the present case and this could be due to the functional groups in N-GQDs. However, the contribution of EM enhancement, if any, cannot be fully ruled out from the above observation.

To ascertain the contribution of the functional groups in the SERS enhancement, N-GQDs substrates are subjected to vacuum annealing at different temperatures (200, 400 and 600 °C) for 2 h to systematically control and eliminate only the functional groups [27,57]. Interestingly, with increasing annealing temperature of N-GQDs substrate, the value of EF of 10^{-4} M RhB for 1648 cm^{-1} peak goes down systematically under 488 nm laser excitation, as shown in Fig. 9(d). The inset shows the corresponding SERS spectra on annealed N-GQDs substrates at different temperatures. The reduction of the functional groups from N-GQDs by vacuum annealing reduces the energy transfer from N-GQDs to RhB in the FRET process. Thus, in the present case, the π–π interaction and the functional groups both contribute to the SERS enhancement on N-GQDs substrate with the RhB target. With 633 nm laser excitation (see Fig. 9(b)), EF is calculated as ~10^2 for 10^{-4} M concentration of RhB at 1648 cm^{-1} peak, which is ~32 times lower than that of the 488 nm excitation. As there is no possibility of FRET between N-GQDs and RhB at 633 nm excitation, the SERS enhancement for 633 nm excitation must be only due to the π–π interaction. Thus, the contribution of FRET to SERS enhancement is only 32 and that of CM is 10^2 yielding an overall enhancement of 3.2×10^3. This confirms the combined contribution of CM interaction and FRET for the observed SERS enhancement with N-GQDs. In the case of undoped GQDs and S-GQDs, due to the low PL intensity, the FRET process is less efficient and hence overall SERS enhancement is low. Moreover, due to higher defect density in GQDs and S-GQDs, the EF is less [3]. Note that due to its semiconducting nature and spherical shape, electromagnetic contribution to the observed SERS in the visible region of wavelength is negligible [58].

Based on the above, the N-GQDs substrate is implemented to detect a very low concentration of RhB in nM level. Fig. 9(e) shows the systematic enhancement of the characteristic Raman peaks of RhB with increasing concentration of RhB in the range 10^{-10}-10^{-4} M. The variation of Raman peak intensity at 1648 cm^{-1} follows a linear nature with the log of RhB concentration, as presented in Fig. 9(f). We achieve a detection limit down to 0.1 nM, which is much superior to the previous reports with GQDs substrate [3,31].

3.4. Applications of N-GQDs for liquid phase WLED fabrication

Since the N-GQDs exhibit strong bluish-green emission with high quantum yield, it is demonstrated here as an excellent light convertor. In the literature, GQDs was used as a light converter in the form of a layer coating [4,59]. The coating of the GQD layer usually gives rise to aggregation-induced quenching of the fluorescence during the deposition of the GQDs solution on to a substrate and the resulting intensity of light emission is low. To avoid the quenching effect, we consider the fabrication of the liquid phase white light LED (WLED) with N-GQDs and then go on to demonstrate WLED with high color purity by combining pink luminescent RhB. The electroluminescence (EL) spectra of the as-prepared UV LED/N-GQD were recorded at different bias voltages in the range 2.79 V–2.97 V, as shown in Fig. S8 (SI†). With increasing bias voltage, the variation of the EL intensity of UV LED centered at 396 nm and the broad PL peak of N-GQDs with a peak at ~503 nm both follow the perfect diode nature (see Fig. 10(a)) in the liquid phase. Fig. 10(b) represents the comparative EL spectra of N-GQDs with the addition of 50 μM RhB at a constant voltage of 2.85 V. Fig. 10(c) represents the Commission International d'E-

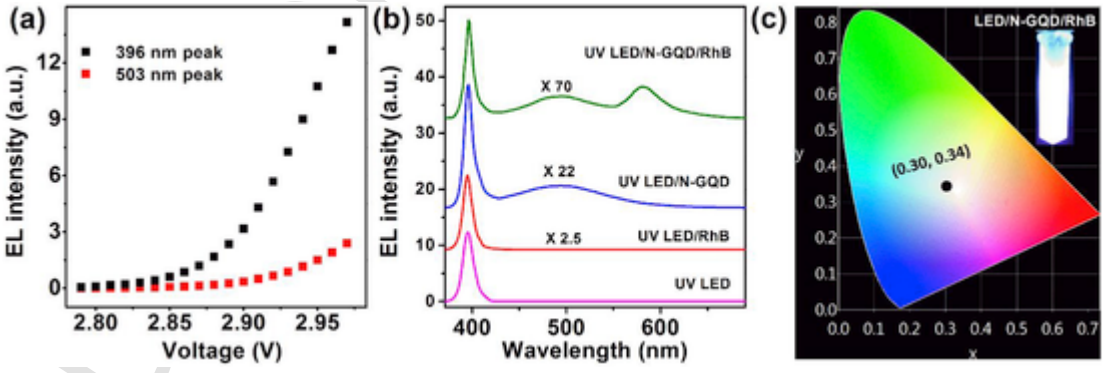

Fig. 10. (a) The EL intensity of UV LED/N-GQD device as a function of bias voltage for emission peaks at 396 nm and 503 nm, which follows the perfect diode nature. (b) The comparison of the EL spectra of UV LED/N-GQD in the absence and presence of 50 μM RhB at 2.85 V. (c) CIE coordinate of UV LED/N-GQDs/RhB system and digital photographs of liquid phase WLED in the inset. (A colour version of this figure can be viewed online.)

clairage (CIE) chromaticity coordinates along with digital photographs of liquid WLED with UV LED/N-GQDs/RhB system. In the N-GQDs medium, the CIE coordinate of UV LED change from (0.1758, 0.0117) to (0.1872, 0.2647), demonstrating the light converting capability of N-GQDs. For the demand of WLED, the addition of RhB with the above system change the CIE coordinate from (0.1872, 0.2647) to (0.3034, 0.3442). White light is produced by inserting the UV LED (396 nm) in the mixed solution of N-GQDs (broad emission with peak maxima at ~503 nm) and RhB (581 nm). Hence, the UV LED is successfully converted into a pure WLED with a mixed solution. With the externally applied voltage, the UV LED excites N-GQDs, which is confirmed from the reduction in the EL intensity at 396 nm by 12.3 times at the applied bias 2.85 V (see Fig. 10(b)). The addition of RhB in the solution of N-GQD reduces the EL intensity ~50 times at 396 nm and increases the visible light emission. Moreover, the EL intensity of N-GQDs at 503 nm is also decreased by ~3 times due to the FRET process. Thus, a series of energy transfer takes place in the following sequence: UV LED to N-GQDs and then to RhB, which establishes N-GQDs as an efficient color converter. By further tuning of the mixing ratio of N-GQDs and RhB, the high purity WLEDs with CIE (0.33, 0.33) could be achieved in the liquid phase. This demonstrates the WLED application of highly fluorescent N-GQDs.

4. Conclusions

In summary, we presented a comparative study of structural and optical features of undoped and doped graphene quantum dots (GQDs) synthesized in water, DMF and DMSO solvents. We proposed that in DMF and DMSO medium, N-GQDs and S-GQDs are formed mainly with nucleophilic reaction, while in water GO sheet is cut in pieces due to the strain caused by the epoxy groups on the basal planes. Different reaction mechanisms in different solvents profoundly affect the size of the GQDs along with their structural and optical properties. The change of the reacting solvents introduces doping content as well as modifies the functional groups in GQDs significantly, as confirmed from the XPS and Raman spectral analysis. Among different undoped and doped GQDs, N-GQDs show the highest PL quantum yield due to the reduction of non-radiative sites at the time of solvent reaction as well as the presence of electron-donating N atoms. On the other hand, the as-synthesized S-GQDs show low PL quantum yield primarily due to the presence of electron-withdrawing S═O functional groups, which act as a non-radiative trap center. Next, we demonstrated N-GQDs as a very efficient SERS substrate based on the energy transfer processes. As a SERS substrate, N-GQDs show SERS enhancement factor up to 3.2×10^3 with 10^{-4} M RhB as a target molecule under 488 nm laser excitation, which is the highest among the reported values. Consequently, it shows an ability to detect RhB with the limit of detection 0.1 nM. The individual contributions of π−π interaction and FRET process in the SERS are evaluated, for the first time, by comparing with different target molecules and laser excitation wavelengths and by controlling the functional groups of GQDs through vacuum annealing. Finally, the highly fluorescent N-GQDs is successfully implemented for the fabrication of a liquid phase white LED with the help of a low-cost UV LED and RhB. These results are significant for the development of low-cost doped GQDs and their applications in SERS and white LEDs.

CRediT authorship contribution statement

Ruma Das: Conceptualization, Methodology, Investigation, Formal analysis, Writing - original draft. **Sumaiya Parveen:** Methodology, Investigation, Formal analysis. **Abhilasha Bora:** Methodology, Investigation, Formal analysis. **P.K. Giri:** Conceptualization, Investigation, Formal analysis, Validation, Writing - review & editing, Supervision, Funding acquisition.

Declaration of competing interest

The authors declare that they have no known competing financial interests or personal relationships that could have appeared to influence the work reported in this paper.

Acknowledgments

We acknowledge the financial support from Meity (Grant No. 5(9)/2012-NANO (VOL-II)) for carrying out part of this work. Central Instruments Facility, I.I.T. Guwahati is acknowledged for providing the TEM, Raman, and TRPL facilities. We gratefully acknowledge Dr. Wolfgang Theis and A. J. Pattison for their help in acquiring the HAADF-STEM images. We thank Dr. H. Sugimoto, Kobe University, Japan, for the support in the XPS measurements.

Appendix A. Supplementary data

Supplementary data to this article can be found online at https://doi.org/10.1016/j.carbon.2020.01.030.

References

[1] R. Das, G. Rajender, P. Giri, Anomalous fluorescence enhancement and fluorescence quenching of graphene quantum dots by single walled carbon nanotubes, Phys. Chem. Chem. Phys. 20 (6) (2018) 4527–4537.
[2] S. Yang, J. Sun, X. Li, W. Zhou, Z. Wang, P. He, et al., Large-scale fabrication of heavy doped carbon quantum dots with tunable-photoluminescence and sensitive fluorescence detection, J. Mater. Chem. A 2 (23) (2014) 8660–8667.
[3] D. Liu, X. Chen, Y. Hu, T. Sun, Z. Song, Y. Zheng, et al., Raman enhancement on ultra-clean graphene quantum dots produced by quasi-equilibrium plasma-enhanced chemical vapor deposition, Nat. Commun. 9 (1) (2018) 193.
[4] L. Tang, R. Ji, X. Cao, J. Lin, H. Jiang, X. Li, et al., Deep ultraviolet photoluminescence of water-soluble self-passivated graphene quantum dots, ACS Nano 6 (6) (2012) 5102–5110.
[5] S. Li, Y. Li, J. Cao, J. Zhu, L. Fan, X. Li, Sulfur-doped graphene quantum dots as a novel fluorescent probe for highly selective and sensitive detection of Fe3+, Anal. Chem. 86 (20) (2014) 10201–10207.
[6] S. Zhu, J. Zhang, S. Tang, C. Qiao, L. Wang, H. Wang, et al., Surface chemistry routes to modulate the photoluminescence of graphene quantum dots: from fluorescence mechanism to up-conversion bioimaging applications, Adv. Funct. Mater. 22 (22) (2012) 4732–4740.
[7] Y. Yang, X. Wang, G. Liao, X. Liu, Q. Chen, H. Li, et al., iRGD-decorated red shift emissive carbon nanodots for tumor targeting fluorescence imaging, J. Colloid Interface Sci. 509 (2018) 515–521.
[8] Z. Chen, C. Wu, Z. Zhang, W. Wu, X. Wang, Z. Yu, Synthesis, functionalization, and nanomedical applications of functional magnetic nanoparticles, Chin. Chem. Lett. 29 (11) (2018) 1601–1608.
[9] P. Zhao, Q. Xu, J. Tao, Z. Jin, Y. Pan, C. Yu, et al., Near infrared quantum dots in biomedical applications: current status and future perspective, WIREs Nanomed. Nanobiotechnol. 10 (3) (2018) e1483.
[10] S. Lu, G. Xiao, L. Sui, T. Feng, X. Yong, S. Zhu, et al., Piezochromic carbon dots with two-photon fluorescence, Angew. Chem. Int. Ed. 56 (22) (2017) 6187–6191.
[11] S. Lu, L. Sui, J. Liu, S. Zhu, A. Chen, M. Jin, et al., Near-infrared photoluminescent polymer–carbon nanodots with two-photon fluorescence, Adv. Mater. 29 (15) (2017) 1603443–1603449.
[12] Q. Wang, S. Zhang, B. Wang, X. Yang, B. Zou, B. Yang, et al., Pressure-triggered aggregation-induced emission enhancement in red emissive amorphous carbon dots, Nanoscale Horiz. 4 (5) (2019) 1227–1231.
[13] Y. Wang, A. Hu, Carbon quantum dots: synthesis, properties and applications, J. Mater. Chem. C 2 (34) (2014) 6921–6939.
[14] R. Das, K.K. Paul, P. Giri, Highly sensitive and selective label-free detection of dopamine in human serum based on nitrogen-doped graphene quantum dots decorated on Au nanoparticles: mechanistic insights through microscopic and spectroscopic studies, Appl. Surf. Sci. 490 (2019) 318–330.

[15] S. Hu, A. Trinchi, P. Atkin, I. Cole, Tunable photoluminescence across the entire visible spectrum from carbon dots excited by white light, Angew. Chem. 54 (10) (2015) 2970–2974.
[16] F.A. Permatasari, A.H. Aimon, F. Iskandar, T. Ogi, K. Okuyama, Role of C–N configurations in the photoluminescence of graphene quantum dots synthesized by a hydrothermal route, Sci. Rep. 6 (2016) 21042.
[17] G. Wang, Q. Guo, D. Chen, Z. Liu, X. Zheng, A. Xu, et al., Facile and highly effective synthesis of controllable lattice sulfur-doped graphene quantum dots via hydrothermal treatment of durian, ACS Appl. Mater. Interfaces 10 (6) (2018) 5750–5759.
[18] D. Qu, Z. Sun, M. Zheng, J. Li, Y. Zhang, G. Zhang, et al., Three colors emission from S,N Co-doped graphene quantum dots for visible light H2 production and bioimaging, Adv. Opt. Mater. 3 (3) (2015) 360–367.
[19] S. Yang, J. Sun, P. He, X. Deng, Z. Wang, C. Hu, et al., Selenium doped graphene quantum dots as an ultrasensitive redox fluorescent switch, Chem. Mater. 27 (6) (2015) 2004–2011.
[20] T. Van Tam, S.G. Kang, K.F. Babu, E.-S. Oh, S.G. Lee, W.M. Choi, Synthesis of B-doped graphene quantum dots as a metal-free electrocatalyst for the oxygen reduction reaction, J. Mater. Chem. A 5 (21) (2017) 10537–10543.
[21] S. Khan, A. Gupta, N.C. Verma, C.K. Nandi, Time-resolved emission reveals ensemble of emissive states as the origin of multicolor fluorescence in carbon dots, Nano Lett. 15 (12) (2015) 8300–8305.
[22] X. Niu, Y. Li, H. Shu, J. Wang, Revealing the underlying absorption and emission mechanism of nitrogen doped graphene quantum dots, Nanoscale 8 (46) (2016) 19376–19382.
[23] S.K. Cushing, M. Li, F. Huang, N. Wu, Origin of strong excitation wavelength dependent fluorescence of graphene oxide, ACS Nano 8 (1) (2013) 1002–1013.
[24] N. Papaioannou, A. Marinovic, N. Yoshizawa, A.E. Goode, M. Fay, A. Khlobystov, et al., Structure and solvents effects on the optical properties of sugar-derived carbon nanodots, Sci. Rep. 8 (1) (2018) 6559.
[25] R. Sekiya, Y. Uemura, H. Naito, K. Naka, T. Haino, Chemical functionalisation and photoluminescence of graphene quantum dots, Chem. Eur J. 22 (24) (2016) 8198–8206.
[26] G. Rajender, U. Goswami, P. Giri, Solvent dependent synthesis of edge-controlled graphene quantum dots with high photoluminescence quantum yield and their application in confocal imaging of cancer cells, J. Colloid Interface Sci. 541 (2019) 387–398.
[27] G. Rajender, P. Giri, Formation mechanism of graphene quantum dots and their edge state conversion probed by photoluminescence and Raman spectroscopy, J. Mater. Chem. C 4 (46) (2016) 10852–10865.
[28] S. Huh, J. Park, Y.S. Kim, K.S. Kim, B.H. Hong, J.-M. Nam, UV/ozone-oxidized large-scale graphene platform with large chemical enhancement in surface-enhanced Raman scattering, ACS Nano 5 (12) (2011) 9799–9806.
[29] P. Wang, M. Xia, O. Liang, K. Sun, A.F. Cipriano, T. Schroeder, et al., Label-free SERS selective detection of dopamine and serotonin using graphene-Au nanopyramid heterostructure, Anal. Chem. 87 (20) (2015) 10255–10261.
[30] J. Ju, W. Liu, C.M. Perlaki, K. Chen, C. Feng, Q. Liu, Sustained and cost effective silver substrate for surface enhanced Raman spectroscopy based biosensing, Sci. Rep. 7 (1) (2017) 6917.
[31] H. Cheng, Y. Zhao, Y. Fan, X. Xie, L. Qu, G. Shi, Graphene-quantum-dot assembled nanotubes: a new platform for efficient Raman enhancement, ACS Nano 6 (3) (2012) 2237–2244.
[32] J.W. Suk, R.D. Piner, J. An, R.S. Ruoff, Mechanical properties of monolayer graphene oxide, ACS Nano 4 (11) (2010) 6557–6564.
[33] T. Dey, S. Mukherjee, A. Ghorai, S. Das, S.K. Ray, Surface state selective tunable emission of graphene quantum dots exhibiting novel thermal quenching characteristics, Carbon 140 (2018) 394–403.
[34] J. Feng, H. Dong, B. Pang, F. Shao, C. Zhang, L. Yu, et al., Theoretical study on the optical and electronic properties of graphene quantum dots doped with heteroatoms, Phys. Chem. Chem. Phys. 20 (22) (2018) 15244–15252.
[35] X. Li, S.P. Lau, L. Tang, R. Ji, P. Yang, Sulphur doping: a facile approach to tune the electronic structure and optical properties of graphene quantum dots, Nanoscale 6 (10) (2014) 5323–5328.
[36] I. Novoa-De León, J. Johny, S. Vázquez-Rodríguez, N. García-Gómez, S. Carranza-Bernal, I. Mendivil, et al., Tuning the luminescence of nitrogen-doped graphene quantum dots synthesized by pulsed laser ablation in liquid and their use as a selective photoluminescence on–off–on probe for ascorbic acid detection, Carbon 150 (2019) 455–464.
[37] Q. Liu, B. Guo, Z. Rao, B. Zhang, J.R. Gong, Strong two-photon-induced fluorescence from photostable, biocompatible nitrogen-doped graphene quantum dots for cellular and deep-tissue imaging, Nano Lett. 13 (6) (2013) 2436–2441.
[38] J.-L. Li, K.N. Kudin, M.J. McAllister, R.K. Prud'homme, I.A. Aksay, R. Car, Oxygen-driven unzipping of graphitic materials, Phys. Rev. Lett. 96 (17) (2006) 176101.
[39] D. Yang, A. Velamakanni, G. Bozoklu, S. Park, M. Stoller, R.D. Piner, et al., Chemical analysis of graphene oxide films after heat and chemical treatments by X-ray photoelectron and Micro-Raman spectroscopy, Carbon 47 (1) (2009) 145–152.
[40] D. Qu, M. Zheng, J. Li, Z. Xie, Z. Sun, Tailoring color emissions from N-doped graphene quantum dots for bioimaging applications, Light Sci. Appl. 4 (12) (2015) e364.
[41] S.H. Jin, D.H. Kim, G.H. Jun, S.H. Hong, S. Jeon, Tuning the photoluminescence of graphene quantum dots through the charge transfer effect of functional groups, ACS Nano 7 (2) (2013) 1239–1245.
[42] A. Das, S. Pisana, B. Chakraborty, S. Piscanec, S.K. Saha, U.V. Waghmare, et al., Monitoring dopants by Raman scattering in an electrochemically top-gated graphene transistor, Nat. Nanotechnol. 3 (4) (2008) 210.
[43] C. Zhu, S. Yang, G. Wang, R. Mo, P. He, J. Sun, et al., Negative induction effect of graphite N on graphene quantum dots: tunable band gap photoluminescence, J. Mater. Chem. C 3 (34) (2015) 8810–8816.
[44] H. Ren, D.D. Kulkarni, R. Kodiyath, W. Xu, I. Choi, V.V. Tsukruk, Competitive adsorption of dopamine and rhodamine 6G on the surface of graphene oxide, ACS Appl. Mater. Interfaces 6 (4) (2014) 2459–2470.
[45] J. Gliniak, J.H. Lin, Y.T. Chen, C.R. Li, E. Jokar, C.H. Chang, et al., Sulfur-doped graphene oxide quantum dots as photocatalysts for hydrogen generation in the aqueous phase, ChemSusChem 10 (16) (2017) 3260–3267.
[46] G. Yang, C. Wu, X. Luo, X. Liu, Y. Gao, P. Wu, et al., Exploring the emissive states of heteroatom-doped graphene quantum dots, J. Phys. Chem. C 122 (11) (2018) 6483–6492.
[47] R. Zhang, J.R. Adsetts, Y. Nie, X. Sun, Z. Ding, Electrochemiluminescence of nitrogen-and sulfur-doped graphene quantum dots, Carbon 129 (2018) 45–53.
[48] S. Parveen, K.K. Paul, R. Das, P. Giri, Large exciton binding energy, high photoluminescence quantum yield and improved photostability of organo-metal halide hybrid perovskite quantum dots grown on a mesoporous titanium dioxide template, J. Colloid Interface Sci. 539 (2019) 619–633.
[49] A. Bora, L.P. Mawlong, R. Das, P. Giri, Understanding the excitation wavelength dependent spectral shift and large exciton binding energy of tungsten disulfide quantum dots and its interaction with single-walled carbon nanotubes, J. Colloid Interface Sci. 561 (2019) 519–532.
[50] S. Santiago, T. Lin, C. Chang, Y. Wong, C. Lin, C. Yuan, et al., Synthesis of N-doped graphene quantum dots by pulsed laser ablation with diethylenetriamine (DETA) and their photoluminescence, Phys. Chem. Chem. Phys. 19 (33) (2017) 22395–22400.
[51] T. Makino, K. Tamura, C. Chia, Y. Segawa, M. Kawasaki, A. Ohtomo, et al., Temperature quenching of exciton luminescence intensity in ZnO/(Mg, Zn) O multiple quantum wells, J. Appl. Phys. 93 (10) (2003) 5929–5933.
[52] P. Yu, X. Wen, Y.-R. Toh, J. Tang, Temperature-dependent fluorescence in carbon dots, J. Phys. Chem. C 116 (48) (2012) 25552–25557.
[53] X. Ling, L. Xie, Y. Fang, H. Xu, H. Zhang, J. Kong, et al., Can graphene be used as a substrate for Raman enhancement?, Nano Lett. 10 (2) (2009) 553–561.
[54] W. Ren, Y. Fang, E. Wang, A binary functional substrate for enrichment and ultrasensitive SERS spectroscopic detection of folic acid using graphene oxide/Ag nanoparticle hybrids, ACS Nano 5 (8) (2011) 6425–6433.
[55] R. Ghosh, J. Ghosh, R. Das, L.P. Mawlong, K.K. Paul, P. Giri, Multifunctional Ag nanoparticle decorated Si nanowires for sensing, photocatalysis and light emission applications, J. Colloid Interface Sci. 532 (2018) 464–473.
[56] R. Swathi, K. Sebastian, Resonance energy transfer from a dye molecule to graphene, J. Chem. Phys. 129 (5) (2008) 054703.
[57] S. Samanta, S. Singh, R.R. Sahoo, Effect of thermal annealing on the physico-chemical and tribological performance of hydrophobic alkylated graphene sheets, New J. Chem. 43 (6) (2019) 2624–2639.
[58] A. Polubotko, V. Chelibanov, The theory of SERS on semiconductor and dielectric substrates, Opt Spectrosc. 122 (6) (2017) 937–943.
[59] G.S. Kumar, U. Thupakula, P.K. Sarkar, S. Acharya, Easy extraction of water-soluble graphene quantum dots for light emitting diodes, RSC Adv. 5 (35) (2015) 27711–27716.